Featured in Physics

Density-Driven Flows in Evaporating Binary Liquid Droplets

A. M. J. Edwards, P. S. Atkinson, C. S. Cheung, H. Liang, D. J. Fairhurst, and F. F. Ouali*
School of Science and Technology, Clifton Lane, Nottingham Trent University, NG11 8NS, Nottingham, United Kingdom

(Received 24 April 2018; revised manuscript received 4 September 2018; published 1 November 2018)

In the evaporation of microlitre liquid droplets, the accepted view is that surface tension dominates and the effect of gravity is negligible. We report, through the first use of rotating optical coherence tomography, that a change in the flow pattern and speed occurs when evaporating binary liquid droplets are tilted, conclusively showing that gravitational effects dominate the flow. We use gas chromatography to show that these flows are solutal in nature, and we establish a flow phase diagram demonstrating the conditions under which different flow mechanisms occur.

DOI: 10.1103/PhysRevLett.121.184501

Flow mechanisms and evaporation dynamics of microparticle laden droplets on solid substrates have been extensively researched due to practical applications including inkjet printing [1], particle self-assembly [2], thin-film coating [3], and biosensors [4]. Most research focuses on single component droplets, revealing an outward radial flow driven by bulk liquid transport towards a pinned contact line [5–7]. However, in many applications, droplets contain two or more liquid components of different volatilities, warranting a detailed understanding of the flow driving mechanisms and the resulting deposition patterns in these more complex solutions [8]. Studies, using several techniques, of evaporating binary droplets, primarily ethanol-water [9–12], show three distinct stages of internal flow: chaotic (stage I), convective (stage II), and outward radial (stage III) [13]. Stage I is characterized by random and strongly circulating vortices, attributed to large surface tension gradients, i.e., solutal Marangoni flows, driven by preferential ethanol evaporation [14]. As ethanol concentration decreases, stage II begins, characterized by a toroidal vortex flowing down the free surface [15,16]. Sefiane *et al.* [9] reported complete evaporation of ethanol by the end of stage I, whereas Lui *et al.* [11], and more recently Chen *et al.* [16], found residual ethanol beyond stage I, consistent with recent numerical simulations [17]. The presence of ethanol within the droplet allows for solutal Marangoni forces to drive convection, although Kang *et al.* [18] suggested buoyancy-driven Rayleigh convection as the driving mechanism. Buoyancy has also been shown to be dominant in evaporating saline droplets on varying wettability surfaces [19–21], but its role in binary liquid droplets is yet to be fully explored. Rayleigh convection within binary droplets is typically excluded due to the 100-fold difference between calculated Marangoni ($\mathrm{Ma}= \Delta\gamma L/\mu D$) and Rayleigh ($\mathrm{Ra}= \Delta\rho g L^3/\mu D$) numbers at small length scales [22]. Here, $\Delta\gamma$ is the surface tension difference, L the characteristic length scale, μ the dynamic viscosity, D the diffusion coefficient in the liquid, $\Delta\rho$ the density difference, and g gravitational acceleration. However, as pointed out by Larson [22], and numerically and experimentally demonstrated by Savino and Fico [23], Marangoni velocities are typically overestimated by a factor of 30, comparable to buoyancy-driven velocities, meaning that buoyancy-driven convection within binary droplets needs to be considered.

In this work, we fully explore the influence of gravity on stage II flow in evaporating binary liquid droplets by systematically tilting the substrate through 180° from sessile to pendant droplets. We measure flow profiles using high speed Fourier domain (FD) optical coherence tomography (OCT). OCT is a Michelson interferometer allowing noncontact 3D imaging of subsurface microstructures. FD-OCT captures the depth profile in one measurement, enabling rapid acquisition of thin cross sections with a larger 3D field of view than microscopy [24], ideal for imaging liquid flow inside droplets. Our 1300-nm center wavelength FD-OCT captures 735 individual depth profiles across a 2.5-mm-wide cross section at 50 fps with a 3D spatial resolution of $13 \times 13 \times 5.5$ μm in air. Droplets and OCT were placed in a $60 \times 60 \times 70$-cm drying enclosure, and a side-view CCD camera was used to record droplet volumes. Both the OCT scan head and droplet were mounted on a rotating stage, maintaining the optical axis perpendicular to the substrate. We used binary solvent mixtures (Table I) with initial concentrations, $2\% \leq c_0 \leq 20\%$, by weight of the more volatile component, to

TABLE I. Physical properties of liquids at 25 °C.

Liquid	ρ (kg/m^3)	γ (mN/m)	Vapor pressure (kPa)
Water	997.1[†]	72.15[†]	3.17[‡]
Ethanol	785.8[†]	22.07[†]	7.87[‡]
n-butanol	805.7[‡]	24.93[‡]	0.86[‡]

[†][25].
[‡][26].

compare the roles of Marangoni and Rayleigh effects in droplets with contact angles, $20° < \theta < 100°$. The Bond number $\mathrm{Bo} = (\rho_l - \rho_v)gL^2/\gamma_L < 1$ gives all droplets a spherical cap.

Figure 1 shows both sessile and pendant cross-section OCT images, averaged over 30 seconds during stage II, of 2 μL droplets with $c_0 = 10\%$ for ethanol-water and water-*n*-butanol. The droplets were seeded with 2-μm polystyrene particles (Sigma-Aldrich) ($\rho = 1.02$ g/cm^3) at 0.01% concentration. For ethanol-water experiments, droplets were placed on a clean glass surface. For water–*n*-butanol experiments, the surface was coated with a nanometer-scale layer of fluoropolymer (Flutech LE15, 3M), increasing θ to be similar to ethanol-water droplets. In OCT images, the optical, rather than physical, path length is measured, explaining the curvature of the droplet-glass interface [24,27].

In both sessile and pendant ethanol-water droplets [Figs. 1(a) and 1(b)], an axisymmetric toroidal vortex flowing upward through the droplet center and down the free surface is observed. In both water–*n*-butanol droplets [Figs. 1(c) and 1(d)], the flow direction is reversed: It is still an axisymmetric toroidal vortex, but it now flows down through the center of the droplet and up the free surface. Flow within evaporating droplets with $\theta < 90°$ is often attributed to the Marangoni effect induced by a surface tension gradient across the interface. This gradient can either be thermal (due to evaporative cooling) or solutal (due to preferential evaporation of one of the components). Expected Marangoni driven flow directions, shown in red in Fig. 1, are independent of droplet orientation. Comparing sessile and pendant droplets in both binary liquids, the flow reverses direction with respect to the substrate or droplet geometry, strongly suggesting that Marangoni effects are not the dominant mechanism driving the flow. Similarly, flow reversal upon droplet inversion excludes any effect of the substrate's thermal conductivity in controlling the flow [29].

For ethanol-water droplets, we estimate solutal $\mathrm{Ma} \sim 1 \times 10^7$ and $\mathrm{Ra} \sim 6 \times 10^4$ at the onset of stage II, assuming pure water at the contact line and bulk ethanol-water at the apex [14], which suggests that Marangoni effects should dominate. However, the clear orientation-dependent flow suggests the influence of buoyancy from density differences due to differential evaporation rates between the two components. In ethanol-water droplets, ethanol rapidly evaporates at the interface, creating a water-rich layer around the droplet, denser than the bulk, which falls due to gravity [19]. In sessile droplets, this drives a flow down the free surface from the apex towards the contact line, in the direction of the expected Marangoni flow. In pendant droplets where the contact line is above the apex, buoyancy induces a flow against the expected Marangoni flow, i.e., from contact line to apex down the free surface (see Fig. 1), as observed experimentally. In water-*n*-butanol, as water preferentially evaporates, the concentration of *n*-butanol increases at the contact line, reducing the density compared to the bulk. In the sessile case, the less dense layer will rise towards the apex, while, in the pendant case, the layer will rise towards the substrate, consistent with observations.

To further explore the role of gravity, we investigated the effect of substrate tilt ϕ (measured anticlockwise) on the flow of ethanol-water droplets. The substrate was coated with Flutech LE15 ($\theta \approx 100°$). Figure 2 shows a selection of results for $c_0 = 2\%$ at $t^* = t/t_f = 0.05$, where t is measurement time and t_f total evaporation time. At $c_0 = 2\%$, droplets start stage II convective flow immediately after deposition, with no stage I chaotic flow.

At $\phi = 0°$ (sessile) [Fig. 2(a)] we observe an axisymmetric toroidal vortex with identical flow direction to the more wetting droplet [Fig. 1(a)]. As ϕ increases to 30°

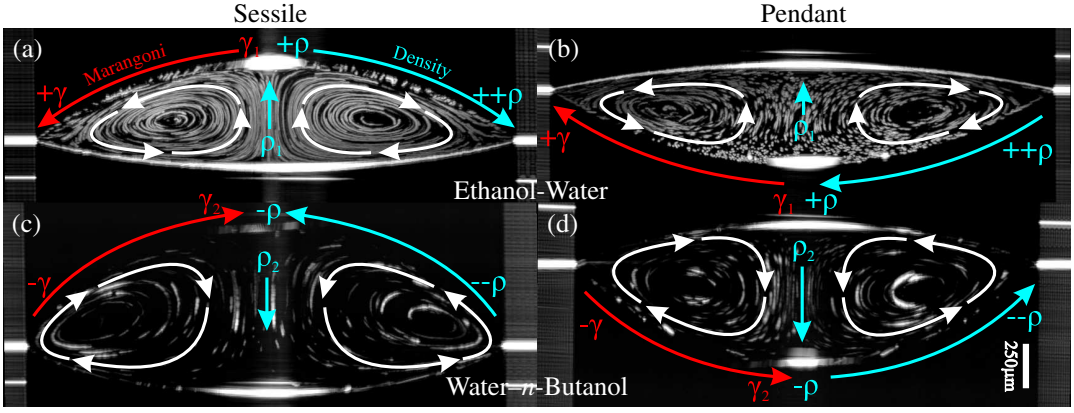

FIG. 1. Time-averaged OCT cross-section images of sessile and pendant 2 μL droplets over 30 seconds of stage II evaporation: (a,b) ethanol-water; (c,d) water-*n*-butanol (see Video 1 in Supplemental Material [28]). Plus and minus signs indicate the expected difference in surface tension (γ) or density (ρ) with respect to the bulk. White arrows indicate observed flow direction. Colored arrows indicate expected flow direction from solutal Marangoni-Rayleigh driven effects. The scale bar shows distance in air.

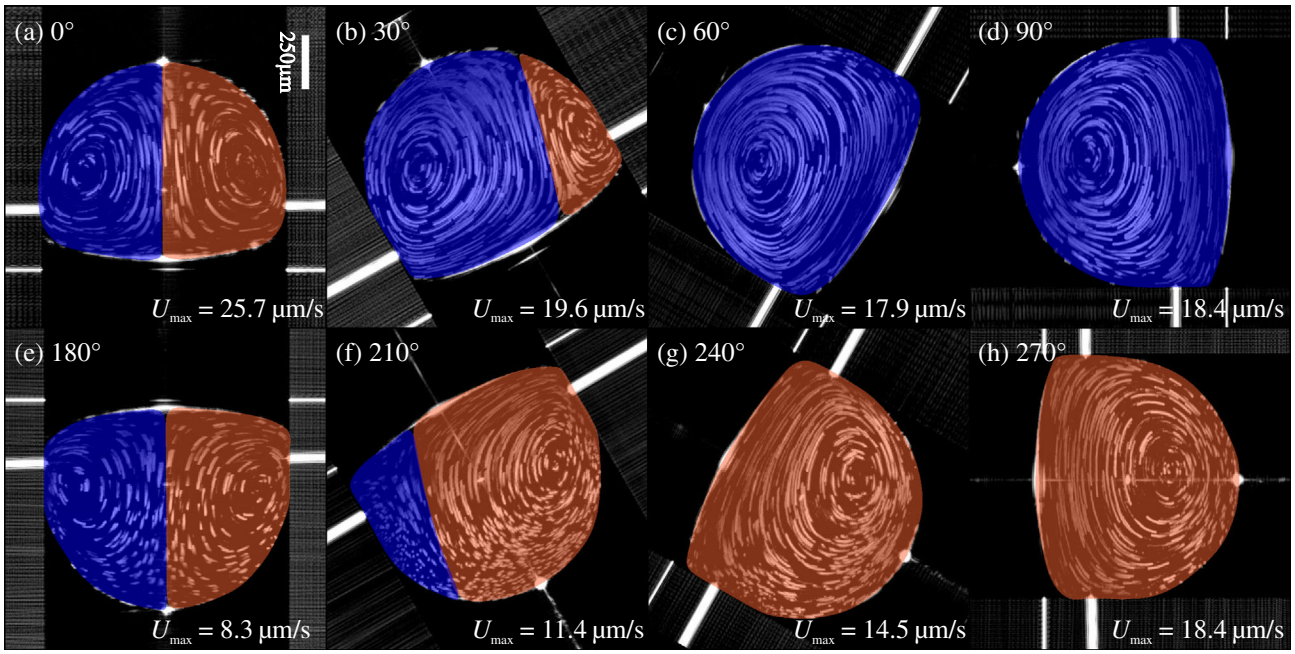

FIG. 2. OCT cross-section images, time averaged over 7 seconds, of 1μL 2% ethanol-water droplets at various substrate tilt angles (see Video 2 in Supplemental Material [28]). Maximum vertical velocity, U_{max} (μm/s), at $t^* = 0.05$ is given in each image. The clockwise (anticlockwise) flow rotation is indicated by brown (blue) shading.

[Fig. 2(b)], the toroidal vortex loses symmetry about the droplet center, becoming larger at the low side and smaller at the high side of the droplet. Since solutal and thermal Marangoni driven flow would be unaffected by tilt, this provides further evidence that buoyancy is driving the flow. For tilts larger than a critical angle, $\phi > \phi_{crit}$, the droplet's highest point is located at or near the contact line, and the flow structure changes from a toroidal vortex to a single-roll cell flowing down the free surface [Figs. 2(c),2(d),2(g), and 2(h)]: Gravity pulls the denser fluid away from the highest point, forming a single-roll cell down the entire free surface. The critical tilt angle scales with contact angle $\phi_{crit} \propto \theta$. As the droplet is tilted back towards the horizontal, but in an upside-down (pendant, $\phi = 180°$) configuration, the flow returns to a toroidal vortex, now flowing away from the solid surface towards the droplet apex [Figs. 2(e) and 2(f)].

We used particle image velocimetry (PIV) [30] to measure the maximum vertical velocity of the liquid flowing towards the droplet apex from its base, U_{max}, at the evaporation time $t^* = 0.05$. This velocity decreases by a factor of 3 from $U_{max} = 25.7$ μm/s at $\phi = 0°$ to $U_{max} = 8.3$ μm/s at 180°. Pradhan *et al.* [19] attributed a similar velocity reduction in evaporating sessile and pendant saline droplets to stratification of the denser liquid at the bottom of the droplet suppressing natural convection. Such stratification is visible at the bottom of the droplet in Figs. 2(e) and 2(f), and is further evidence of the role of gravity within evaporating binary liquid droplets.

Previous studies demonstrate that buoyancy driven convection in the vapor phase can increase droplet evaporation [31,32]. However, we do not believe that vapor flow plays a significant role in controlling flow for two reasons. First, gas viscosity is several orders of magnitude lower than the liquid's, so flow in the vapor phase should have a negligible effect on flow within the droplet [33,34]. Second, were vapor convection responsible for fluid flow, we would expect a flow reversal in the later stages of evaporation as ethanol vapor (sinking over the free surface) is replaced by water vapor (rising over the free surface). Such flow reversal was not observed in any experiments. Therefore, we discount any effects of vapor flow influencing fluid flow.

The images in Figs. 1 and 2 show conclusively that the flow in stage II of an evaporating binary droplet depends on the droplet's orientation with respect to gravity, in turn demonstrating the importance of density variations in controlling the flow. To quantify the driving mechanism, we used gas chromatography (GC) to measure the average concentration throughout the evaporation of 11 identical 10-μL sessile ethanol-water droplets, dispensed 12 cm apart within the enclosure. One of the droplets was continuously monitored using OCT. The other droplets, assumed to be evaporating similarly, were removed at various times, transferred into vials, and immediately sealed for subsequent GC analysis, allowing a measurement of the average ethanol concentration at the moment of removal, $c(t^*)$. Figure 3(a) shows corresponding results of GC and PIV experiments.

GC analysis of $c_0 = 5\%$ and 10% droplets found $c(t^*)$ to be well approximated by $c(t^*) = c_0 \exp(-Bt^*)$, with $B = 12 \pm 0.5$ [Fig. 3(a) inset] [12,16]. Similarly, side-camera

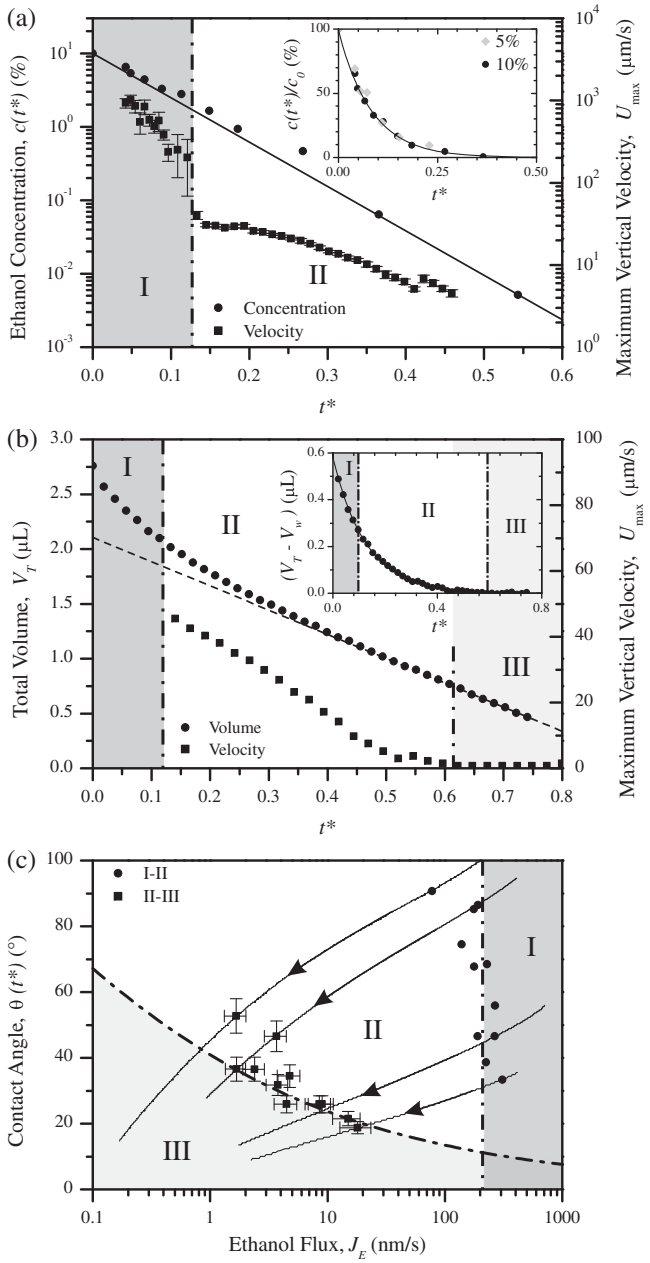

FIG. 3. (a) GC-determined ethanol concentration $c(t^*)$ and maximum vertical velocity ($U_{\max}$) vs t^* for $c_0 = 10\%$. The solid line is an exponential fit to the data. (b) Variation of total droplet volume (V_T) and $U_{\max}$ with t^* for $c_0 = 20\%$. The inset shows an exponential decrease of ethanol volume with t^*. (c) Phase diagram showing the three stages characterized by ethanol flux (J_E) and contact angle $\theta(t^*)$ at t^*.

measurements of volume and PIV analysis of a smaller 2.76-μL droplet with $c_0 = 20\%$ [Fig. 3(b) and Video 3 in Supplemental Material [28]) show that, as stage III begins (identified by $U_{\max} = 0$), the evaporation rate is nearly constant, as expected for the evaporation of a pure water droplet $dV_T/dt \approx dV_w/dt \approx 1.4 \times 10^{-3}$ μL/s [dashed line in Fig. 3(b)]. Subtracting the extrapolated water volume V_w from the total droplet volume V_T, we estimate the volume of ethanol, V_E, within the droplet [Fig. 3(b) inset]. The extracted value of V_E follows a similar exponential decay as obtained from GC analysis in larger droplets, indicating that volume analysis can be used to reliably determine ethanol concentration within smaller, non-GC suitable droplets. For volume estimated droplets, $B = 9.2 \pm 1.2$. This slight reduction in B suggests that initial ethanol concentration and volume slightly influence the rate of ethanol evaporation. We find that at the stage I-II transition, ethanol is still present [Figs. 3(a) and (b)], consistent with the experiments of Chen *et al.* [16] and simulations of Diddens *et al.* [17], indicating that the convective flow can be attributed to solutal differences across the droplet. As stage II progresses, $c(t^*)$ continues decreasing exponentially, reducing the solutal differences, thereby decreasing the overall driving force leading to a reduction in $U_{\max}$ and to a transition into stage III when $U_{\max} = 0$.

We discussed earlier that the traditional dimensionless numbers (Ma and Ra) are insufficient to describe when buoyancy influences flow. An alternative approach is needed. To help guide future research into this topic and to better understand the flow transitions, in Fig. 3(c) we trace droplet evaporation trajectories on a $\theta(t^*)$ vs J_E phase diagram, where $J_E = (dV_E/dt)/A$ is the ethanol flux (A is the droplet surface area). The arrowed black lines are experimentally determined trajectories for four droplets ($c_0 = 20\%$) with fixed radius but different initial volumes. Solid symbols mark measured stage I-II (circles) and stage II-III (squares) transitions for 11 droplets. The I-II transition is determined by a sharp drop in $U_{\max}$ [see Fig. 3(a)], whereas the II-III transition is determined by $U_{\max} = 0$, which is more difficult to determine precisely [see Fig. 3(b)], hence the larger corresponding error in t^*, and also in J_E and $\theta(t^*)$.

For the measured contact angles ($33° < \theta < 88°$), the I-II transition occurs at a roughly constant value of ethanol flux $J_E^* = 210 \pm 6$ nm/s [dash-dotted vertical line in Fig. 3(c)], suggesting a critical evaporation flux at which the flow changes from chaotic to convective (I-II). The stage II-III transition has a dependence on both J_E and $\theta(t^*)$, with lower contact angle droplets transitioning at higher J_E. Using Fick's law to determine the density difference between the surface and bulk $\Delta\rho = J_E h(\delta\rho/\delta c)/D$, we find that $\mathrm{Ra} = J_E g(\delta\rho/\delta c)h^4/\mu D^2$. Calculating this value at the II-III transition for all droplets gives a critical Rayleigh number, $\mathrm{Ra}^* = 43 \pm 3$, plotted as the curved dash-dotted line in Fig. 3(c), which, despite significant scatter, captures the II-III boundary shape. The small value of Ra* is consistent with predictions of Dash *et al.* [35]. From our calculations, droplets with $c_0 = 2\%$, shown in Fig. 2, have an initial $J_E \approx 31$ nm/s $< J_E^*$, placing them in the convective regime at the moment of deposition, consistent with observations.

We next propose a physical mechanism to account for the seeming dominance of buoyancy despite Ma $\gg$ Ra.

Consider a sessile ethanol-water droplet with $\theta = 90°$ and uniform evaporation so that a water-enriched layer develops evenly. No Marangoni flow will ensue as $\Delta\gamma$ is zero across a compositionally uniform surface. However, the higher density of the layer compared to the bulk causes it to fall down the free surface, initiating Rayleigh convection. A rising plume of bulk fluid refreshes the ethanol at the interface, reducing surface tension and inducing a Marangoni flow in the direction of Rayleigh flow. Typically, such convective replenishing is ignored in calculations of $\Delta\gamma$ and hence Ma, explaining the literature's overestimation of surface tension effects. The argument holds for other θ, with nonuniform evaporation across the surface, provided that convection dominates over diffusion, as measured by the product of Reynolds and solutal Prandtl numbers, $\mathrm{PrRe} = U_{\max} h/D \gg 1$, throughout stage II. For pendant droplets, bulk fluid is transported to the contact line; again, Marangoni flow will reinforce Rayleigh convection.

In this Letter, we report the development of rotatable OCT imaging to explore convective flow patterns within tilted evaporating binary liquid droplets on substrates with $20° \leq \theta \leq 100°$, conclusively demonstrating that, in contrast to current view and conventional calculation of Ma and Ra, stage II is driven by Rayleigh convection. Our result prompts a reconsideration of current explanations of flow mechanisms within multicomponent droplets and emphasizes the importance of considering convective replenishing before calculating Marangoni stresses. We use GC to directly measure the time evolution of ethanol concentration within droplets and confirm that a simple analysis of volume data provides the same information. Finally, we use the dynamic concentration data to construct a phase diagram, showing that stage I chaotic flow ends when the ethanol evaporation flux drops below a critical value and stage II convective flow transitions to outward radial flow below a critical value of Ra.

The authors acknowledge R. E. Hill for initial experiments and L. Goehring for helpful discussions. A. M. J. E. acknowledges financial support from Nottingham Trent University.

*Corresponding author.
fouzia.ouali@ntu.ac.uk

[1] H. Sirringhaus, T. Kawase, R. Friend, T. Shimoda, M. Inbasekaran, W. Wu, and E. Woo, Science **290**, 2123 (2000).
[2] W. Han and Z. Lin, Angew. Chem., Int. Ed. Engl. **51**, 1534 (2012).
[3] M. Layani, M. Gruchko, O. Milo, I. Balberg, D. Azulay, and S. Magdassi, ACS Nano **3**, 3537 (2009).
[4] J. R. Trantum, M. L. Baglia, Z. E. Eagleton, R. L. Mernaugh, and F. R. Haselton, Lab Chip **14**, 315 (2014).
[5] R. D. Deegan, O. Bakajin, T. F. Dupont, G. Huber, S. R. Nagel, and T. A. Witten, Nature (London) **389**, 827 (1997).
[6] H. Hu and R. G. Larson, J. Phys. Chem. B **110**, 7090 (2006).
[7] A. Marin, R. Liepelt, M. Rossi, and C. J. Kähler, Soft Matter **12**, 1593 (2016).
[8] J. Park and J. Moon, Langmuir **22**, 3506 (2006).
[9] K. Sefiane, L. Tadrist, and M. Douglas, Int. J. Heat Mass Transfer **46**, 4527 (2003).
[10] A. K. Cheng, D. M. Soolaman, and H.-Z. Yu, J. Phys. Chem. B **110**, 11267 (2006).
[11] C. Liu, E. Bonaccurso, and H.-J. Butt, Phys. Chem. Chem. Phys. **10**, 7150 (2008).
[12] J. R. E. Christy, Y. Hamamoto, and K. Sefiane, Phys. Rev. Lett. **106**, 205701 (2011).
[13] X. Zhong and F. Duan, Eur. Phys. J. E **39**, 18 (2016).
[14] R. Bennacer and K. Sefiane, J. Fluid Mech. **749**, 649 (2014).
[15] H. Kim, F. Boulogne, E. Um, I. Jacobi, E. Button, and H. A. Stone, Phys. Rev. Lett. **116**, 124501 (2016).
[16] P. Chen, M. Toubal, J. Carlier, S. Harmand, B. Nongaillard, and M. Bigerelle, Langmuir **32**, 9836 (2016).
[17] C. Diddens, J. G. Kuerten, C. van der Geld, and H. Wijshoff, J. Colloid Interface Sci. **487**, 426 (2017).
[18] K. H. Kang, S. J. Lee, C. M. Lee, and I. S. Kang, Meas. Sci. Technol. **15**, 1104 (2004).
[19] T. K. Pradhan and P. K. Panigrahi, Colloids Surf. **530**, 1 (2017).
[20] K. H. Kang, H. C. Lim, H. W. Lee, and S. J. Lee, Phys. Fluids **25**, 042001 (2013).
[21] R. Savino and R. Monti, J. Cryst. Growth **165**, 308 (1996).
[22] R. G. Larson, AIChE J. **60**, 1538 (2014).
[23] R. Savino and S. Fico, Phys. Fluids **16**, 3738 (2004).
[24] S. Manukyan, H. M. Sauer, I. V. Roisman, K. A. Baldwin, D. J. Fairhurst, H. Liang, J. Venzmer, and C. Tropea, J. Colloid Interface Sci. **395**, 287 (2013).
[25] I. S. Khattab, F. Bandarkar, M. A. A. Fakhree, and A. Jouyban, Korean J. Chem. Eng. **29**, 812 (2012).
[26] D. Lide, *CRC Handbook of Chemistry and Physics* (CRC Press, Boca Raton, 2003).
[27] S. Lawman and H. Liang, Appl. Opt. **50**, 6039 (2011).
[28] See Supplemental Material at http://link.aps.org/supplemental/10.1103/PhysRevLett.121.184501 for supplementary videos.
[29] W. D. Ristenpart, P. G. Kim, C. Domingues, J. Wan, and H. A. Stone, Phys. Rev. Lett. **99**, 234502 (2007).
[30] W. Thielicke and E. Stamhuis, J. Open Res. Software **2**, e30 (2014).
[31] Z. Pan, S. Dash, J. A. Weibel, and S. V. Garimella, Langmuir **29**, 15831 (2013).
[32] R. Savino, D. Paterna, and N. Favaloro, J. Thermophys. Heat Transfer **16**, 562 (2002).
[33] C. Bouchenna, M. Aitsaada, S. Chikh, and L. Tadrist, J. Phys. Conf. Ser. **925**, 012006 (2017).
[34] C. Diddens, H. Tan, P. Lv, M. Versluis, J. Kuerten, X. Zhang, and D. Lohse, J. Fluid Mech. **823**, 470 (2017).
[35] S. Dash, A. Chandramohan, J. A. Weibel, and S. V. Garimella, Phys. Rev. E **90**, 062407 (2014).